Materials Chemistry and Physics 358 (2026) 132484

Contents lists available at ScienceDirect

Materials Chemistry and Physics

journal homepage: www.elsevier.com/locate/matchemphys

Full length article

Defect-mediated ionic polarization and transport crossover in cold-sintered $CsPbI_3$

Manish Kumar [a], Pardeep K. Jha [b], Priyanka A. Jha [c,*], Prabhakar Singh [d,*]

[a] Department of Physics, School of Sciences, IFTM University, Moradabad 244102, UP, India
[b] Disorder and Transport Physics Lab, School of Basic and Applied Sciences, K.R. Mangalam University Gurugram, Gurugram 122103, Haryana, India
[c] Materials Physics Laboratory, Department of Physics and Materials Science & Engineering, Jaypee University, Anoopshahr (Bulandshahr) 203390, UP, India
[d] Department of Physics, Indian Institute of Technology (Banaras Hindu University), Varanasi 221005, India

HIGHLIGHTS

- Cold-sintered orthorhombic $CsPbI_3$ exhibits scan-dependent dc transport hysteresis.
- Low-field nonlinearity originates from ionic polarization and defect redistribution.
- Dielectric spectra show strong conductive loss without Debye-type relaxation.
- Grain and grain-boundary transport are resolved using Jonscher power-law analysis.
- Modulus spectroscopy reveals defect-mediated relaxation distinct from dc conduction.

ARTICLE INFO

Keywords:
Perovskite halides
Ionic polarization
Dielectric relaxation
Hysteresis
Electric modulus

ABSTRACT

Orthorhombic $CsPbI_3$ synthesized via cold sintering solid-state reaction was investigated to elucidate its dc transport and dielectric relaxation behavior. Current density–electric field (j–E) measurements under dark and AM 1.5G illumination exhibit near-ohmic conduction at higher fields with pronounced scan-direction–dependent hysteresis, indicating polarization- and ion-migration–assisted transport. A deviation from ideal ohmic behavior at low electric fields ($E < 1$ kVm^{-1}), particularly in the reverse scan, reflects slow ionic redistribution and non-equilibrium internal fields. Dielectric spectroscopy reveals strong low-frequency dispersion without a distinct loss peak, indicating non-Debye relaxation associated with distributed ionic dynamics. Frequency-dependent ac conductivity analyzed using the Jonscher power law reveals two transport regimes and a transport crossover near 377 K with reduced activation energies. Complementary electric modulus analysis confirms multiple relaxation processes with characteristic times lying in the range of 20–150 μs and comparatively higher activation energies associated with localized defect relaxation. The combined dc and ac transport analyses demonstrate that defect-mediated ionic dynamics, rather than a crystallographic phase transition, govern hysteresis and dielectric dispersion in $CsPbI_3$.

1. Introduction

All-inorganic halide perovskites with a general formula of $CsPbX_3$, (where X = Cl, Br, and I) have emerged as a material of significant interest for optoelectronic and photovoltaic applications owing to their large absorption coefficients, long diffusion lengths of charge carriers, and appropriate band gaps for solar energy harvesting [1–3]. Compared to organic–inorganic hybrid perovskites, $CsPbX_3$ compounds exhibit superior thermal stability due to the replacement of volatile organic cations with inorganic cesium ions, making them more attractive for long-term device operation [4,5]. Among this family, $CsPbI_3$ has attracted particular attention because of its favorable band gap (~1.7 eV), excellent optoelectronic properties, and potential for high power conversion efficiencies, making it particularly relevant for single-junction and tandem photovoltaic architectures [6–9]. However, the optically active black perovskite phase of $CsPbI_3$ is metastable at room temperature and tends to transform into the orthorhombic yellow phase, which represents the thermodynamically stable ground state of the material [10,11]. Recent advances in synthesis strategies, including solid-state and solution-based approaches, as well as surface and lattice engineering, have improved the stabilization of $CsPbI_3$ and

* Corresponding author.
E-mail addresses: priyankajha.dce@gmail.com, priyanka.jha@mail.jaypeeu.ac.in (P.A. Jha), psingh.app@iitbhu.ac.in (P. Singh).

https://doi.org/10.1016/j.matchemphys.2026.132484
Received 13 January 2026; Received in revised form 17 March 2026; Accepted 1 April 2026
Available online 2 April 2026

enhanced its thermal and operational stability [10–15]. Despite these advances, the intrinsic defect chemistry and phase instability of $CsPbI_3$ remain critical challenges, motivating continued investigation of its fundamental transport properties [5].

Beyond structural and optical considerations, defect-mediated ionic polarization and defect migration have emerged as an important factor governing the electrical response of halide perovskites. The migration of mobile ionic species under internal electric fields and illumination leads to slow polarization accumulation that dynamically couples with electronic charge transport, giving rise to time-dependent effects such as current–voltage hysteresis [14–16]. Previous studies have demonstrated that slow ionic motion, with diffusion coefficients on the order of $\sim 10^{-12}$ cm^2 s^{-1}, can reproduce experimentally observed hysteresis and non-linear transport behavior in halide perovskites [17,18]. These findings highlight that charge transport in $CsPbI_3$ cannot be described solely by electronic conduction, as ionic redistribution alters internal electric field profiles and modulates carrier extraction and recombination pathways [19]. Furthermore, the interaction between mobile ionic defects and electronic carriers has been shown to produce diverse hysteresis behaviors across different perovskite compositions, underscoring the sensitivity of transport phenomena to defect chemistry and ion mobility [20,21].

Recent transport studies on related halide perovskites such as $CsPbBr_3$ and Cu-based iodide ($CuPbI_3$,$CuSnI_3$) perovskites have shown that dc current–voltage characteristics often deviate from ideal ohmic behavior at low electric fields, accompanied by scan-direction-dependent conduction regimes arising from ionic polarization and space-charge effects [22–24]. In these systems, illumination-assisted halide migration and field-dependent dielectric relaxation have been shown to modify current response and the apparent onset of non-linear conduction. Such observations suggest that low-field transport anomalies are not purely electronic in origin but are closely linked to slow ionic redistribution and polarization dynamics [25–27]. In this context, dielectric spectroscopy provides a powerful complementary approach by probing frequency- and temperature-dependent relaxation processes associated with mobile defects and dipolar entities [28–30]. Combined analysis of ac conductivity dispersion and electric modulus formalism enables separation of bulk and interfacial contributions and provides insight into defect-mediated relaxation dynamics in disordered ionic systems [31–33].

In the present work, polycrystalline $CsPbI_3$ was synthesized via a cold-sintering solid-state reaction route, stabilizing the orthorhombic yellow phase. Although this phase is optically inactive for photovoltaic absorption [6] due to its wide band gap, it represents the thermodynamic ground state into which the black perovskite phase transforms during degradation; moreover, illumination can still influence charge transport through defect-mediated photo-conductivity and enhanced ionic redistribution, making this phase a suitable platform for investigating intrinsic defect-driven ionic transport processes. To the best of our knowledge, a systematic correlation between low-field dc transport nonlinearity, ac conductivity dispersion, and electric modulus relaxation in orthorhombic $CsPbI_3$ has not been previously reported. Here, we systematically investigate its dc transport behavior and dielectric response over a wide temperature range by combining current–electric field measurements, ac conductivity analysis, and electric modulus spectroscopy. The results reveal pronounced low-field nonlinearity and relaxation dynamics associated with defect-driven ionic polarization. By correlating conductivity dispersion with modulus relaxation, we observe a transport crossover around ~377 K that arises from coupled ionic–electronic processes and defect redistribution rather than a crystallographic phase transition. These findings provide insight into polarization-controlled transport mechanisms in halide perovskites and help clarify the role of ionic defects in governing charge transport stability.

2. Materials and methods

2.1. Sample preparation

Cesium iodide (CsI, 99.9%) was procured from Sigma Aldrich, while lead iodide (PbI_2) was synthesized as described in our earlier article [34]. Perovskite powder $CsPbI_3$ was synthesized by solid-state reaction route via cold sintering method at room temperature. Stoichiometric amounts of CsI and PbI_2 were thoroughly mixed and ground for 2 h in an agate mortar under ambient conditions (relative humidity ~60%). During grinding, the precursor mixture gradually transformed into a yellow-colored powder, indicating the formation of the orthorhombic polymorph of $CsPbI_3$. The obtained powder was uniaxially pressed into pellets using a hydraulic press and subsequently sintered in a vacuum oven at 80 °C for 1 h to improve densification and grain connectivity. The circular pellets with a thickness of ~1 mm and a diameter of ~11.5 mm were used for electrical characterization after silver electroding on both face.

2.2. Characterization techniques

The identification of the phase formation for the compounds was investigated by the X-ray diffraction (XRD) technique using Rigaku-Miniflex. The surface morphology images and Energy Dispersive X-ray analysis (EDX) of the sample were obtained using EVO - Scanning Electron Microscope MA15/18. The optical absorption spectrum of the synthesized material was examined by the JASCO V-770 Ultraviolet-Visible spectrometer. The thermodynamical studies of the compounds were performed using SHIMADZU DSC-60 plus 230 V. The X-ray photoelectron spectroscopy (XPS) spectra were measured employing KRATOS (Amicus model) using the Mg target under 10^{-6} Pa pressure. The current (I) - Voltage (V) characteristic was performed in Dark and with regular exposure the Science tech solar simulator class: AAA under solar illumination AM 1.5 G using Keithley 2450 source meter up to 3 h. An electrical contact was established using gold-coated Z-pin probes in a through-thickness configuration. Before IV measurement, the two electrodes were briefly shorted with a metallic wire to remove any residual surface charge and to ensure a neutral initial state. No external poling field was applied. Several preliminary voltage sweeps (typically ~5 to 10) were performed until the current–voltage response became stable and reproducible; the data reported in the manuscript correspond to the stabilized response. The voltage was swept in dual-scan mode from −5 V to +5 V. The sweep was performed at a constant scan rate of 1.66 V s^{-1} in continuous mode without an additional programmed dwell time at each bias point. Dielectric and impedance measurements of the studied perovskite material was done using Solartron 1260 A impedance analyzer at 1 V over a wide frequency (10^{-1} to 10^6 Hz) and temperature range (297 to 457 K). Prior to it, AC amplitude is varied in 0.0001 V to 1 V.

3. Results and analysis

The $CsPbI_3$ synthesized by the cold sintering method crystallizes in the yellow polymorph of $CsPbI_3$(supplementary, Fig.S1). Rietveld analysis confirmed the orthorhombic structure with space group *Pnma* and lattice parameter (in Å) 10.471622, 4.804939 and 17.798300. The microstructure exhibits well-connected grains with an average grain size ~ 0.51 μm. UV study suggests an optical band gap of ~2.33 eV(supplementary, Fig.S2–S4). X-ray photoelectron spectroscopy (XPS) was performed to examine the chemical composition of the constituent elements. The survey and high-resolution spectra of Cs 3d, Pb 4f, and I 3d along with the estimated elemental composition comparison with EDX are provided in Fig.S5 (supplementary figure). Although this yellow polymorph is structurally stable at room temperature, preliminary current–voltage measurements reveal a near-linear transport response accompanied by degradation under prolonged light exposure

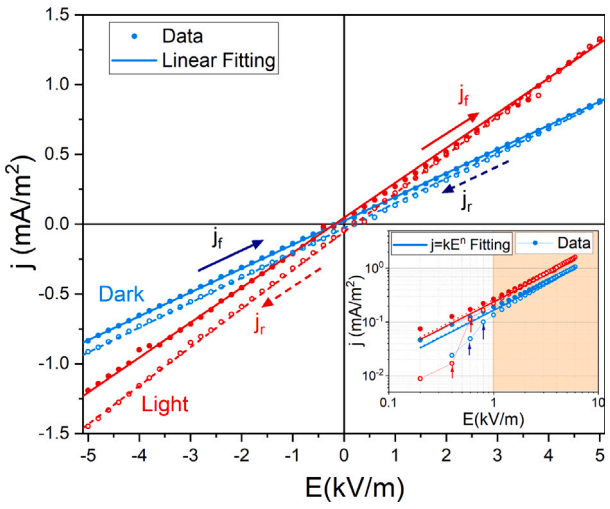

Fig. 1. Linear-scale current density–electric field (j–E) characteristics of $CsPbI_3$ measured under dark and AM 1.5G illumination conditions during forward (j_f) and reverse (j_r) voltage sweeps. A near-linear response with clear hysteresis is observed, indicating polarization- and ion-migration–assisted transport. The inset shows the corresponding log–log representation with phenomenological power-law fitting $j = kE^n$, yielding an exponent n close to unity, suggesting weak field-assisted conduction. Illumination leads to a significant increase in the prefactor k, reflecting enhanced free-carrier density, while the transport exponent remains nearly unchanged.

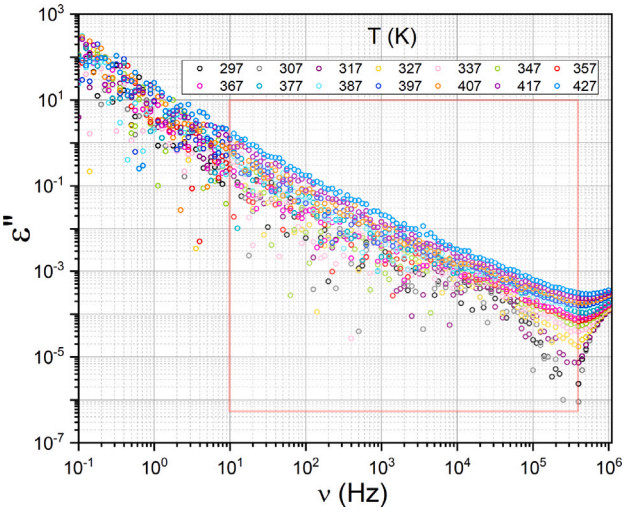

Fig. 2. Bode representation of the imaginary permittivity (ε'') as a function of frequency at various temperatures for $CsPbI_3$. The pronounced low-frequency dispersion reflects dc conductivity and interfacial/ionic polarization effects with temperature.

(supplementary, Fig.S6) [34]. To elucidate the origin of the observed current–voltage hysteresis and instability in the yellow phase, a detailed investigation of charge carrier transport and ionic dynamics was undertaken.

3.1. DC transport and current–voltage hysteresis

The current density–electric field (j–E) characteristics measured under dark and AM 1.5 G illumination (light) conditions for forward and reverse voltage sweeps are shown in Fig. 1. The measurements were performed in the linear single-slope voltage–time regime (graph not shown) over an applied electric field range from −5 to +5 kVm^{-1}. The forward (j_f) and reverse (j_r) scans (Fig. 1) exhibit a nearly linear response ($R^2 > 0.999$) with a clear hysteresis, indicating polarization- and ion-migration-assisted transport. Using microscopic Ohm's law, $j = \sigma E$; the electrical conductivity was estimated. The conductivity shows a marginal increase in the reverse scan (~0.18 and 0.28 μSm^{-1}) compared to the forward scan (~0.17 and 0.25 μSm^{-1}) under dark and light conditions, respectively.

To gain further insight, the j–E curves were analyzed on a log–log scale (Fig. 1, inset) using the power-law relation [24,29],

$$j = kE^n \tag{1}$$

where k is prefactor and n is exponent. For all scans, the exponent $n \sim 1$ (Max.(Δn) < 10^{-4} and $R^2 > 0.99$), indicating nearly ohmic transport. Under these conditions, the prefactor k effectively corresponds to the electrical conductivity σ, and its magnitude agrees well with the conductivity values obtained from linear ohmic fitting.

However, an important feature is observed at low electric fields (E < 1 kVm^{-1}), where a deviation from ideal ohmic behavior appears. While a linear ohmic relation holds for all scans in the high-field regime (E > 1 kVm^{-1}), slight deviations are observed for the forward scan at low fields on the log–log scale. This deviation is more pronounced for the reverse scan under both dark and illumination conditions, suggesting the presence of polarization-assisted transport and non-equilibrium internal electric fields [35]. However, due to the limited number of data points in this low-field regime, quantitative fitting is not attempted.

These observations indicate that the transport behavior in $CsPbI_3$ is strongly influenced by field-dependent polarization and slow ionic processes. The dc current–voltage measurements alone are insufficient to disentangle the respective contributions of electronic transport, ionic drift, and interfacial polarization, particularly in materials exhibiting slow relaxation dynamics [30,31]. Dielectric spectroscopy provides a powerful complementary probe by accessing frequency (ν) and temperature (T) dependent polarization and relaxation processes [32]. The imaginary part of the complex permittivity, $\varepsilon''(\nu, T)$ may be expressed as [32,33]

$$\varepsilon''(\nu, T) = \frac{\sigma_{dc}(T)}{\nu \varepsilon_0} + \chi''(\nu, T) \tag{2}$$

where the first term represents the contribution from dc conductivity (σ_{dc}) and the second term, $\chi''(\nu, T) \simeq \varepsilon''_{relax}(\nu, T)$ accounts for relaxation processes associated with dipolar entities or mobile defects. Analysis of dielectric loss spectra, together with ac conductivity dispersion and electric modulus formalism, enables discrimination between distributed relaxation times, hopping-dominated transport, and grain versus grain-boundary contributions while suppressing electrode polarization effects. To elucidate the origin of the observed hysteresis and scan-dependent conduction, dielectric spectroscopy was employed and is discussed in the following section.

3.2. Frequency- and temperature-dependent permittivity dispersion

Preliminary dielectric measurements performed at lower AC excitation amplitudes exhibited significant data scatter (see supplementary, Fig.S7), particularly at low frequencies. This behavior is consistent with the enhanced current fluctuations observed in the low-field region of the dc j–E characteristics (Fig. 1). Such fluctuations are attributed to slow ionic migration and interfacial polarization processes that dominate charge transport under weak electric fields. To obtain stable and reproducible dielectric spectra, an AC excitation amplitude of 1 V was therefore selected. This amplitude remains within the quasi-ohmic transport regime, as confirmed by the linear j–E response at comparable field strengths.

To investigate the polarization and relaxation mechanisms, temperature-dependent Bode plots of the dielectric loss permittivity ($\varepsilon\varepsilon$) are presented in Fig. 2. The frequency-dependent dielectric loss ($\varepsilon\varepsilon$) exhibits a pronounced low-frequency dispersion that approximately

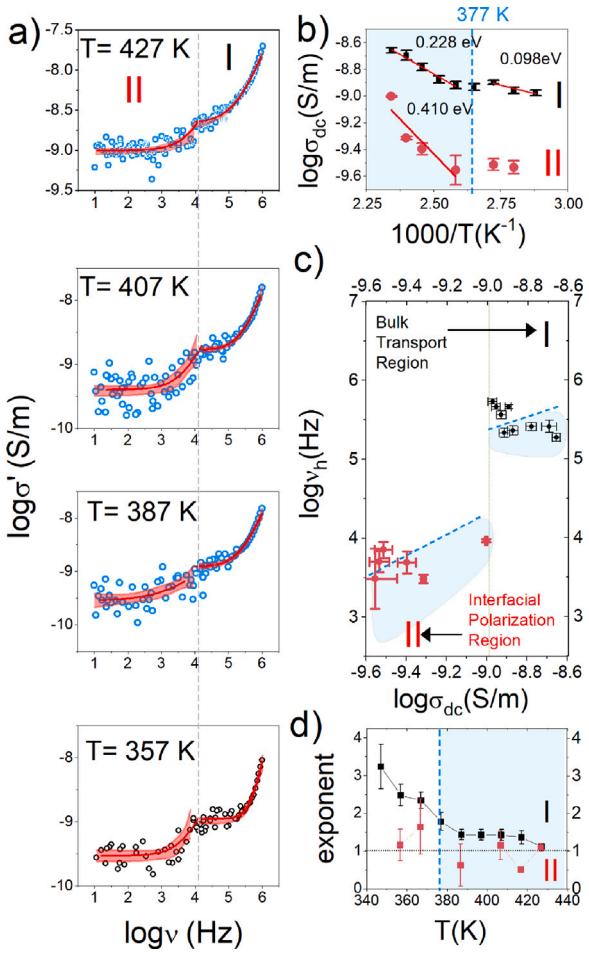

Fig. 3. (a) Frequency-dependent ac conductivity spectra (σ') at 357 K, 387 K, 407 K, and 427 K, fitted (red lines with 95% confidence bands) using the Jonscher power law to extract the dc conductivity (σ_{dc}). The dashed vertical line marks the crossover frequency separating the dc plateau (I: Bulk dominated transport region) and dispersive regimes (II: Interfacial polarization dominated region). (b) Arrhenius plots of the extracted dc conductivity with errors bars showing distinct activation energies associated with bulk transport (I) and interfacial polarization (II) dominated regimes. Blue dashed line represents 377 K and the shaded blue region is for data corresponds to $T > 377$ K (c) Log–log correlation between the hopping frequency (ν_h) and the dc conductivity (σ_{dc}). Two clusters are observed corresponding to bulk-dominated transport (region I) and interfacial polarization (region II). Dashed lines are guides to the eye indicating the distinct scaling trends in the two regimes. (d)Temperature dependence of the Jonscher exponent (n). The thin horizontal line indicates $n = 1$, separating sub-linear and superlinear dispersion regimes. The shaded region highlights the higher-temperature regime ($T > 377$ K).

follows a ν^{-1}-like dependence across the measured range, indicating a dominant contribution from dc conductivity and electrode/space-charge polarization effects [31]. Accordingly, the dielectric response can be expressed using Eq. (2), where the first term represents the conductive loss arising from long-range charge transport, while the second term accounts for polarization-related dielectric relaxation processes associated with localized defect dynamics.

Notably, no well-defined loss peak is observed within the accessible frequency window (10^{-1}–10^{6} Hz), ruling out a simple Debye-type dipolar relaxation. Instead, the dielectric loss shows a gradual, temperature-dependent variation in magnitude with only weak indications of peak shifting. This behavior is consistent with slow ionic motion and a broad distribution of relaxation times. Such a response suggests that the dielectric behavior of $CsPbI_3$ is governed by coupled ionic–electronic dynamics rather than a single, well-defined dipolar relaxation, in agreement with the hysteresis and scan-dependent dc transport behavior discussed earlier.

3.3. Frequency-dependent conductivity and activation energy

The absence of a well-defined dielectric loss peak within the measured frequency window, together with the indication of a broad distribution of relaxation times, suggests that the dielectric response is dominated by conductivity-related processes. To further elucidate the transport mechanism, the frequency-dependent conductivity spectra were therefore analyzed using the Jonscher universal power-law formalism to quantitatively extract the dc conductivity (σ_{dc}).

The frequency-dependent conductivity spectra exhibit two characteristic regions: a frequency-independent dc plateau at low frequencies and a dispersive region at higher frequencies. The ac conductivity spectra were measured in the temperature range 297–427 K. Fig. 3(a) shows the variation of log σ' as a function of log ν (conductivity isotherms) at representative temperatures of 357, 387, 407, and 427 K for $CsPbI_3$.

In general, conductivity isotherms consist of a well-defined low-frequency plateau corresponding to dc conduction, followed by a frequency-dependent dispersion at higher frequencies. In the present case, the low-frequency plateau exhibits noticeable scatter, while the high-frequency region shows a systematic increase with frequency. The scattered nature of the low-frequency region indicates incomplete long-range charge transport, likely arising from slow ionic motion and interfacial polarization effects. In contrast, the high-frequency dispersion reflects localized hopping dynamics of charge carriers, consistent with previously reported behavior in ionically active halide perovskites [24–27].

To analyze the conduction mechanism, the conductivity isotherms are fitted with the Jonscher universal power law (JPL) [31,32]:

$$\sigma'(\nu) = \sigma_{dc} + A\nu^{n'} \tag{3}$$

where σ_{dc} represents the zero-frequency limit of $\sigma'(\nu)$. A is a temperature-dependent pre-exponential factor, and n' is the frequency exponent characterizing the dispersive transport.

The conductivity spectra reveal two frequency regimes, separated by a characteristic crossover frequency (marked by a vertical dashed line). Regime I corresponds to the high-frequency regime (10^4–10^6 Hz), where the response is dominated by localized bulk transport processes, whereas Regime II corresponds to the low-frequency region (10–10^4 Hz), where interfacial polarization and electrode-related effects become significant. The absence of a well-defined dc plateau in the Regime II indicates suppression of long-range hopping due to charge accumulation and potential barriers at interfaces.

The dc conductivity values extracted from the JPL fitting curves were used to construct Arrhenius plots, (Fig. 3(b)), using relation ($\sigma_{dc} = \sigma_0 exp(-E_a/k_B T)$) Where, σ_0, E_a, K, and T are the pre-exponential factor, activation energy, Boltzmann constant, and absolute temperature, respectively. Linear fitting of log σ_{dc} vs 1000/T yields distinct activation energies. Above the transport anomaly near 377 K (shaded region), the activation energies are ~0.228 eV for Regime I and ~0.41 eV for Regime II. Below this temperature, the activation energies decrease to ~0.098 eV for Regime I. For Regime II, only a qualitative trend toward lower activation energy is inferred, as reliable fitting is not possible due to the limited number of data points. This behavior indicates enhanced charge mobility at elevated temperatures. This reduction in activation energy is consistent with thermally activated migration of iodine-related point defects, such as iodine interstitials (I_i), which reduce the effective energy barrier for charge transport at elevated temperatures [24,25,36,37].

To further examine the hopping dynamics, the relationship between σ_{dc} and the characteristic hopping frequency ν_h are was analyzed for both regimes (Fig. 3(c)). Although, the data exhibit noticeable scatter, two clusters are distinguishable corresponding to the

two transport regimes. A further separation of the data is observed around the crossover temperature ~377 K (blue dashed line). For the data extracted from isotherms $T < 377$ (shaded zone), a relatively weak dependence between σ_{dc} and the characteristic hopping frequency ν_h is observed. It suggests that charge transport is dominated by localized defect-related relaxation processes. In contrast, for $T > 377$ K a clearer correlation emerges, indicating thermally activated hopping transport where increased conductivity is accompanied by higher hopping frequencies.

This behavior correlates with the temperature dependence of the Jonscher exponent n', shown in Fig. 3(d). The exponent n' decreases with increasing temperature but remains greater than unity, indicating superlinear frequency-dependent conduction. While the classical universal dielectric response predicts $0 < n < 1$, superlinear dispersion ($n' > 1$) has been reported in disordered ionic conductors [38] where correlated ion motion, defect–dipole interactions, and interfacial polarization can modify the simple hopping dynamics. In the present system, the defect-rich microstructure and mobile ionic defects may contribute to such non-ideal dispersive behavior.

The change in activation energy and the concomitant stabilization of the Jonscher exponent near ~377 K suggest a modification in the dominant charge transport dynamics. To verify whether this feature originates from a structural phase transition, differential scanning calorimetry (DSC) measurements were performed between 275–475 K. No detectable thermal event was observed in the investigated temperature range, indicating the absence of a structural transformation. The DSC thermogram and its first derivative are provided in Fig. S8 (Supplementary figure). Therefore, the feature near ~377 K is attributed to a transport crossover in ionic dynamics rather than a phase transition. To examine whether this transport crossover manifests in the dielectric response, the temperature-dependent permittivity was analyzed at different frequencies.

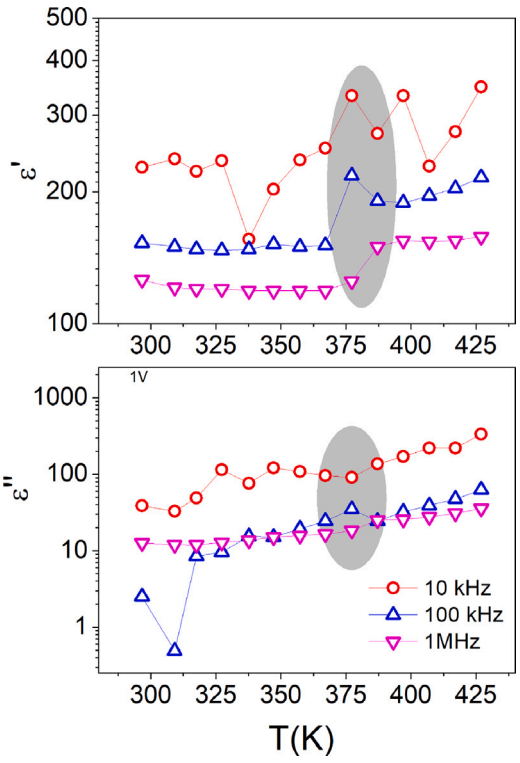

Fig. 4. Variation of ε' and ε'' (real and imaginary parts of permittivity, respectively) are plotted with the temperature at 10 kHz, 100 kHz, and 1 MHz frequencies.

3.4. Temperature-dependent dielectric response

The real (ε') and imaginary (ε'') parts of permittivity are plotted as a function of temperature at 10 kHz, 100 kHz, and 1 MHz frequencies (Fig. 4). Both ε' and ε'' are constant up to ~370 K above which a kink is observed followed by new plateau (gray region). The anomaly is centered around ~377 K, closely coinciding with the change in slope observed in the activation-energy analysis of the conductivity spectra (Fig. 3).

Importantly, the dielectric response exhibits a clear frequency dependence without any divergence or well-defined loss peak across the investigated temperature range. The absence of a sharp anomaly rules out a conventional ferroelectric, structural, or order–disorder phase transition. Instead, the observed dielectric feature is indicative of a relaxation-type process associated with thermally activated redistribution of ionic defects.

The correlated changes in activation energy, Jonscher exponent, and dielectric permittivity near ~377 K therefore signify a transport crossover. This transport crossover likely originates from defect reconfiguration and enhanced ionic mobility, which modify the balance between localized hopping and long-range transport pathways. Such a transport-driven anomaly provides a consistent framework for understanding the observed dc hysteresis and low-frequency dielectric dispersion in $CsPbI_3$.

3.5. Modulus relaxation and activation energy

To further elucidate the nature of the relaxation processes underlying the observed transport crossover, the electric modulus formalism was employed. The absence of a well-defined relaxation peak in the dielectric loss spectra indicates that the response is dominated by conductivity-related polarization processes, which tend to mask intrinsic bulk relaxation features in the permittivity representation. In such cases, the electric modulus formalism provides a more suitable framework for analyzing relaxation dynamics because it suppresses electrode polarization effects and emphasizes bulk processes associated with localized charge carrier motion [32,39]. Accordingly, the frequency-dependent response was analyzed using the electric modulus representation.

To confirm two contributions in ac conductivity isotherms we have studied the modulus Bode plots (i.e., modulus loss spectrum $M''(\omega)$, where $\omega = 2\pi\nu$) . The $M''(\omega)$ isotherms (300 to 427 K) were fitted using the Debye, Cole–Cole and Cole–Davidson Models [31,32] (See supplementary, Fig.S9) according to the following expressions:

$$M''(\omega) = \frac{M_\infty \omega\tau}{1 + (\omega\tau)^2} \tag{4}$$

$$M''(\omega) = \frac{M_\infty (\omega\tau)^{1-\alpha} sin(\frac{\alpha\pi}{2})}{1 + 2(\omega\tau)^{1-\alpha} cos(\frac{\alpha\pi}{2}) + (\omega\tau)^{2(1-\alpha)}} \tag{5}$$

$$M''(\omega) = \frac{M_\infty sin[\beta tan^{-1}(\omega\tau)]}{\left(1 + (\omega\tau)^2\right)^{\beta/2}} \tag{6}$$

Fig. 5 summarizes the modulus analysis and the corresponding relaxation dynamics. Fig. 5(a), shows a representative modulus loss spectrum at 427 K along with Debye, Cole–Cole, and Cole–Davidson fittings. The Debye model fails to reproduce the asymmetric shape of the experimental peak, particularly in the high-frequency regime suggesting the presence of multiple relaxation times.

The statistical fitting improves significantly when the Cole–Cole, and Cole–Davidson models are employed. The temperature dependence of the symmetric broadening parameter, $'\alpha'$ (Cole–Cole) and asymmetric parameters, $'\beta'$ (Cole–Davidson) is shown in Fig. 5(b). Although the Cole–Cole model improves the fit by introducing the symmetric broadening of the relaxation peak, the extracted symmetric broadening parameter, $\alpha > 1$, which is beyond physical acceptance ($0 < \alpha < 1$). Thus, Cole–Cole model is rejected. In contrast, the Cole–Davidson

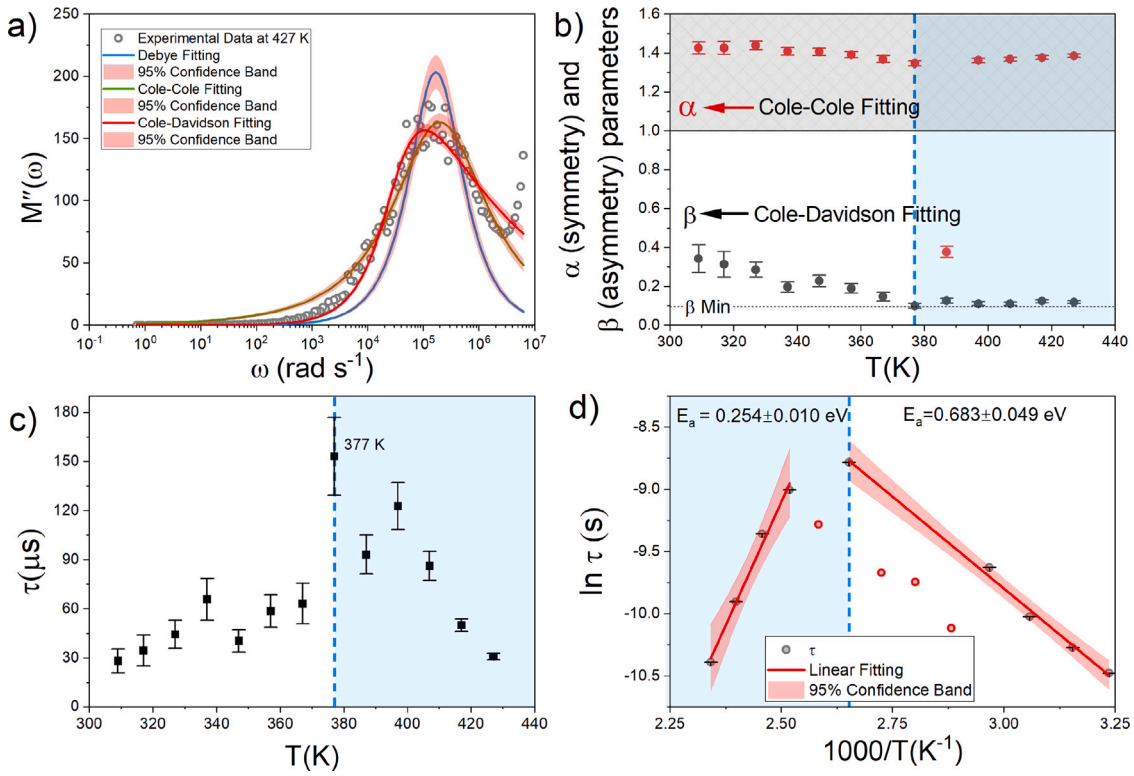

Fig. 5. (a) Modulus loss spectrum M″(ω) plot of $CsPbI_3$ at 427 K showing fits using Debye, Cole–Cole, and Cole–Davidson relaxation models. The shaded bands represent 95% confidence intervals for the respective fits. (b) Temperature dependence of the Cole–Cole symmetry parameter α and Cole–Davidson asymmetry parameter β. The unphysical values $\alpha > 1$ indicate that the Cole–Cole model does not adequately describe the relaxation process, whereas the Cole–Davidson model provides physically meaningful parameters. (c) Relaxation time τ extracted from Cole–Davidson fitting as a function of temperature. (d) Arrhenius representation of the relaxation time showing two activation regimes separated near 377 K. The shaded region indicates the high-temperature regime.

model yields the best agreement with the experimental data across the entire frequency range. Also, asymmetric parameters, $'\beta'$ remains within the physically acceptable range and exhibits values between approximately 0.1 and 0.35, consistent with a strongly asymmetric distribution of relaxation times typically observed in disordered ionic systems.

The relaxation time, τ, extracted from the Cole–Davidson fitting, is shown as a function of temperature in Fig. 5(c). A noticeable change in behavior is observed near $T \sim 377$ K, suggesting a crossover in the relaxation dynamics. This temperature also coincides with the minimum value of the asymmetry parameter, β_{min} (indicated by horizontal dashed line) in Fig. 5(b). The relaxation time, τ, lies in the range of ~20 to 150 μs. To further examine the thermally activated nature of the relaxation process, the activation energy is estimated from the Arrhenius plots for activation energy (variation of $ln(\tau)$ vs $1000/T$, Fig. 5(d)). Two distinct linear regimes are observed, yielding activation energies of $E_a = 0.254\pm0.010$ eV above the crossover temperature and $E_a = 0.683\pm0.049$ eV below the crossover temperature. The coincidence of this crossover temperature with the anomaly observed in the ac conductivity analysis further supports the presence of a transition in the dominant charge relaxation mechanism.

The higher activation energies obtained from electric modulus analysis indicate that the observed relaxation processes are associated with localized defect rearrangement and short-range ionic motion within the bulk rather than long-range charge transport. Such relaxation is governed by the reorientation of defect–dipole complexes and migration of ionic defects under thermally activated conditions. In the Pb- poor conditions, different defect species are expected to dominate in different temperature regimes. Accordingly, at lower temperatures the relaxation process is attributed primarily to the formation and migration of lead vacancies (V''_{Pb}) associated with the higher activation energy of ~0.683 eV whereas at elevated temperatures iodine vacancies ($V^{\bullet}_{I}$) become increasingly mobile, giving rise to a lower activation energy of ~0.254 eV [24,25,36,37].

The apparent disparity between the activation energies extracted from conductivity and electric modulus analyses reflects the fundamentally different transport processes probed by these techniques. Conductivity measurements are sensitive to long-range charge transport [32], whereas electric modulus spectroscopy is more sensitive to bulk dielectric relaxation associated with localized defect dynamics. A notable observation is that above the crossover temperature (~377 K), the activation energy obtained from bulk conductivity (0.228 eV) becomes comparable to that derived from modulus relaxation (0.254 eV). This close agreement suggests that both long-range conduction and dielectric relaxation are governed by the same thermally activated hopping process at elevated temperatures, most plausibly associated with the migration of mobile iodine-related defects.

In contrast, below the crossover temperature the activation energies extracted from the two techniques differ substantially. The modulus relaxation exhibits a higher activation energy (~0.683 eV), indicating localized defect rearrangement and short-range ionic motion within the bulk lattice. Meanwhile, conductivity measurements reveal a much lower effective activation energy (~0.098 eV), implying that long-range transport occurs through lower-barrier percolative pathways, likely influenced by interfacial regions and defect-assisted hopping. The presence of Pb deficiency indicated by XPS measurements (Fig S5) supports the possibility of vacancy-related defect complexes contributing to the localized relaxation behavior at lower temperatures.

The low-temperature synthesis route employed in this work (mechanical grinding followed by mild annealing at ~80 °C) may also influence the defect landscape and interfacial structure of $CsPbI_3$. Unlike conventional high-temperature solid-state reactions that promote defect equilibration and grain growth, the cold-sintering approach can preserve a higher density of non-equilibrium defects and interfacial

regions. Such a defect-rich micro-structure is known to facilitate ionic motion and space-charge accumulation in halide perovskites, which may contribute to the pronounced low-frequency dielectric dispersion and interfacial contributions observed in the present study.

Conclusively, the convergence of activation energies at higher temperatures and their pronounced disparity at lower temperatures indicate a redistribution of dominant transport pathways near ~377 K. This behavior is consistent with a transport crossover in which the dominant mechanism evolves from localized defect relaxation at lower temperatures to thermally activated ionic hopping at elevated temperatures. The absence of any thermal anomaly in DSC measurements further confirms that this crossover feature arises from defect-mediated transport processes rather than a crystallographic phase transition. These results highlight the critical role of defect-mediated ionic dynamics in governing charge transport and dielectric relaxation in orthorhombic $CsPbI_3$.

4. Conclusion

This study establishes that electrical hysteresis and low-field nonlinearity in orthorhombic $CsPbI_3$ originate from defect-driven ionic processes that coexist with predominantly ohmic electronic transport. The combined dc conductivity, dielectric, and electric modulus analyses reveal that long-range charge transport is governed by thermally activated iodine-related defects, whereas localized relaxation dynamics arise from higher-energy defect reorientation processes within the bulk lattice. The transport crossover observed near ~377 K reflects a redistribution of dominant transport pathways and relaxation dynamics. The absence of any thermal anomaly in the DSC measurements rules out a crystallographic phase transition in this temperature range. Interfacial regions act as space-charge barriers that hinder long-range transport, resulting in larger effective activation energies compared to bulk conduction. Importantly, the divergence between activation energies extracted from conductivity and modulus formalism's highlights the necessity of employing complementary spectroscopic techniques to disentangle conduction and relaxation phenomena in halide perovskites. These findings underscore the critical role of ionic dynamics and polarization in determining transport stability in all-inorganic perovskites and provide a framework for interpreting hysteresis and degradation mechanisms beyond dc measurements alone.

CRediT authorship contribution statement

Manish Kumar: Writing – review & editing, Writing – original draft, Methodology, Formal analysis, Data curation. **Pardeep K. Jha:** Writing – review & editing, Visualization, Investigation, Formal analysis. **Priyanka A. Jha:** Writing – review & editing, Writing – original draft, Validation, Supervision, Methodology, Investigation, Formal analysis, Data curation, Conceptualization. **Prabhakar Singh:** Writing – review & editing, Supervision, Project administration, Funding acquisition.

Declaration of competing interest

The authors declare that they have no known competing financial interests or personal relationships that could have appeared to influence the work reported in this paper.

Acknowledgments

This work is supported by DST, India (CRG/2018/001926) India. PAJ is thankful to BRNS project 58/14/17/2025-BRNS/760.

Appendix A. Supplementary data

See Supplementary material for Fig. S1–S9.

Supplementary material related to this article can be found online at https://doi.org/10.1016/j.matchemphys.2026.132484.

Data availability

All data that support the findings of this study are included within the article (and any supplementary files).

References

[1] J. Zhang, G. Hodes, Z. Jin, S. Liu, All-inorganic CsPbX3 perovskite solar cells: progress and prospects, Angewandte Chem. Int. Ed. 58 (2019) 15596–15618.
[2] X. Zhang, P. Yang, CsPbX3 (X= Cl, Br, and I) nanocrystals in substrates toward stable photoluminescence: Nanoarchitectonics, properties, and applications, Langmuir 39 (2023) 11188–11212.
[3] B. Chaudhary, Y.K. Kshetri, H-S. Kim, et al., Current status on synthesis, properties and applications of CsPbX3 (X= Cl, Br, I) perovskite quantum dots/nanocrystals, Nanotechnology 32 (2021) 502007.
[4] H. Wang, Z. Dong, H. Liu, et al., Roles of organic molecules in inorganic CsPbX3 perovskite solar cells, Adv. Energy Mater. 11 (2021) 2002940.
[5] N. Pai, D. Angmo, Powering the future: Opportunities and obstacles in lead-halide inorganic perovskite solar cells, Adv. Sci. 12 (2025) 2412666.
[6] Z. Yao, W. Zhao, S.F. Liu, Stability of the $CsPbI_3$ perovskite: from fundamentals to improvements, J. Mater. Chem. A 9 (2021) 11124–11144.
[7] M. Maqbool, G. Rehman, L. Ali, et al., Structural, electronic and optical properties of $CsPbX_3$(X=Cl, Br, I) for energy storage and hybrid solar cell applications, J. Alloys Compd. 705 (2017) 828–839, http://dx.doi.org/10.1016/j.jallcom.2017.02.147.
[8] D. Liu, Z. Shao, C. Li, et al., Structural properties and stability of inorganic $CsPbI_3$ perovskites, Small Struct. 2 (2021) 2000089.
[9] Y. Wang, Y. Chen, T. Zhang, et al., Chemically stable black phase $CsPbI_3$ inorganic perovskites for high-efficiency photovoltaics, Adv. Mater. 32 (2020) 2001025.
[10] G.E. Eperon, G.M. Paternò, R.J. Sutton, A. Zampetti, A.A. Haghighirad, F. Cacialli, H.J. Snaith, Inorganic caesium lead iodide perovskite solar cells, J. Mater. Chem. A 3 (39) (2015) 19688–19695, http://dx.doi.org/10.1039/C5TA06398A.
[11] Y. Liu, Small hole polarons in yellow phase δ−$CsPbI_3$, Phys. Rev. Mater. 9 (6) (2025) 065402, http://dx.doi.org/10.1103/yr22-9j6r.
[12] L. Sirna, A.L. Pellegrino, L. Pulvirenti, et al., Simple and environmentally friendly solution synthesis of $CsPbI_3$ nanoribbons: Investigating the reversible δ-to γ-phase transition, Adv. Photonics Res. (2025) e202500059.
[13] Y. Wang, H. Zhao, M. Piotrowski, et al., Cesium lead iodide perovskites: optically active crystal phase stability to surface engineering, Micromachines 13 (2022) 1318.
[14] H. Yao, J. Zhao, Z. Li, et al., Research and progress of black metastable phase $CsPbI_3$ solar cells, Mater. Chem. Front. 5 (2021) 1221–1235.
[15] B. Wang, F. Zhang, R. Lv, et al., Enhancing the stability of red-emitting $CsPbI_xBr_{3-x}$ QDs for advanced display applications, Nanoscale 17 (2025) 24404–24426.
[16] J. Han, S. Qin, H. Liu, et al., Illumination regulated ion migration in metal halide perovskite, J. Phys. Chem. Lett. 16 (2025) 10042–10048.
[17] S. Kumar, R.K. Sahu, External electric field induced atomic charge migration and surface degradation of $CsPbI_3$: A reactive molecular dynamics simulation based study, Mater. Chem. Phys. 333 (2025) 130350.
[18] X. Liu, P. Zeng, S. Chen, et al., Charge transfer dynamics at the interface of $CsPbX_3$ perovskite nanocrystal-acceptor complexes: A femtosecond transient absorption spectroscopy study, Laser Photonics Rev. 16 (2022) 2200280.
[19] L. Bertoluzzi, R.A. Belisle, K.A. Bush, et al., In situ measurement of electric-field screening in hysteresis-free PTAA/FA0. 83Cs0. 17Pb (I0. 83Br0. 17) 3/C60 perovskite solar cells gives an ion mobility of~ 3× 10–7 cm2/(V s), 2 orders of magnitude faster than reported for metal-oxide-contacted perovskite cells with hysteresis, J. Am. Chem. Soc. 140 (2018) 12775–12784.
[20] S. Tammireddy, M.N. Lintangpradipto, O. Telschow, et al., Hysteresis and its correlation to ionic defects in perovskite solar cells, J. Phys. Chem. Lett. 15 (2024) 1363–1372.
[21] G.L. Nogueira, V. Lopez-Richard, L.A. Meneghetti Jr., et al., A new approach to characterize charge transport and hysteresis in perovskite solar cells, 2025, arXiv preprint arXiv:250210805.
[22] J. Shi, X. Xu, H. Zhang, et al., Intrinsic slow charge response in the perovskite solar cells: Electron and ion transport, Appl. Phys. Lett. 107 (2015).
[23] G. Xia, B. Huang, Y. Zhang, et al., Nanoscale insights into photovoltaic hysteresis in triple-cation mixed-halide perovskite: resolving the role of polarization and ionic migration, Adv. Mater. 31 (2019) 1902870.
[24] M. Kumar, P.A. Jha, P.K. Jha, P. Singh, Hysteric photo-conduction and negative differential resistance in cesium lead bromide, J. Appl. Phys. 127 (2020) http://dx.doi.org/10.1063/5.0012202.
[25] P.C. Bharti, P.K. Jha, P.A. Jha, P. Singh, Hysteresis in centrosymmetric $CuPbI_3$ perovskite halide: Apolar dielectric or orientable dielectric? J. Phys. Condens. Matter 33 (2021) http://dx.doi.org/10.1088/1361-648X/abdb67.
[26] P.C. Bharti, P.K. Jha, S. Singh, et al., Exploring phase transition effects on current voltage hysteresis in novel CuSnI 3, Phys. B Condens. Matter 715 (2025) http://dx.doi.org/10.1016/j.physb.2025.417434.

[27] N.F. Mott, R.W. Gurney, Electronic Processes in Ionic Crystals, first ed., Oxford University Press, 1940.
[28] M.A. Lampert, Simplified theory of space-charge-limited currents in an insulator with traps, Phys. Rev. 103 (1956) 1648–1656, http://dx.doi.org/10.1103/PhysRev.103.1648.
[29] K.C. Kao, Dielectric Phenomena in Solids, Academic Press/Elsevier, San Diego, 2004.
[30] S.R. Elliott, A.c. conduction in amorphous chalcogenide and pnictide semiconductors, Adv. Phys. 36 (1987) 135–217, http://dx.doi.org/10.1080/00018738700101971.
[31] A.K. Jonscher, Dielectric relaxation in solids, J. Phys. D Appl. Phys. 32 (1999) R57–R70, http://dx.doi.org/10.1088/0022-3727/32/14/201.
[32] A.K. Jonscher, Dielectric Relaxation in Solids, Chelsea Dielectrics Press, London, 1983.
[33] R.K. Dwivedi, P.K. Jha, P.A. Jha, P. Kumar, Structural - electrical property correlation in defect induced nanostructured off-stoichiometric bismuth ferrite: A defect analysis, Mater Chem. Phys. 164 (2015) 15–22, http://dx.doi.org/10.1016/j.matchemphys.2015.08.012.
[34] M. Kumar, V. Pawar, P.A. Jha, et al., Thermo-optical correlation for room temperature synthesis: cold-sintered lead halides, J. Mater. Sci., Mater. Electron. 30 (2019) 6071–6081, http://dx.doi.org/10.1007/s10854-019-00908-x.
[35] A.K. Ranjan, P.A. Jha, P.K. Jha, P. Singh, Anisotropic photoconduction in ultrathin CuO: A nonreciprocal system? J. Appl. Phys. 132 (2022) http://dx.doi.org/10.1063/5.0116696.
[36] M. Wierzbowska, A. Mikłas, Preserving bond ionicity under illumination to achieve photostable halide perovskites, J. Phys. Chem. C 127 (2023) 3750–3759, http://dx.doi.org/10.1021/acs.jpcc.2c08110.
[37] Y. Liang, F. Li, X. Cui, et al., Toward stabilization of formamidinium lead iodide perovskites by defect control and composition engineering, Nat. Commun. 15 (2024) 1707, http://dx.doi.org/10.1038/s41467-024-46044-x.
[38] D. Kumar, A.S. Bangwal, S. Singh, P.A. Jha, P. Singh, High –temperature conduction mechanism of samarium ferrite substituted sodium niobate ceramics, Phys. B 582 (2020) 412028, http://dx.doi.org/10.1016/j.physb.2020.412028.
[39] P.K. Jha, P.A. Jha, V. Singh, et al., Diffuse phase ferroelectric vs. Polomska transition in (1-x)BiFeO3-(x)BaZr0.025Ti0.975O3 ($0.1 \leq x \leq 0.3$) solid solutions, J. Appl. Phys. 117 (2015) http://dx.doi.org/10.1063/1.4905715.